Gradient-Based Multi-Objective Beam Pattern Synthesis for RIS-Assisted 6G Networks

Nguyen Thi Toan[1, 2], Nguyen Cong Minh[2], Truong Vu Bang Giang[3], Nguyen Minh Tran[2*]
[1]Hai Duong University, Hai Phong, Vietnam
[2]VNU University of Engineering and Technology, Hanoi, Vietnam
[3]Vietnam National University, Hanoi, Vietnam
[*]*Corresponding author: Nguyen Minh Tran*, Email: minhtran.nguyen@vnu.edu.vn

***Abstract*—Pattern synthesis in reconfigurable intelligent surface (RIS)-assisted systems presents a formidable non-convex optimization challenge, particularly when implemented through phase-only control of the reflective elements. This paper proposes an advanced optimization framework leveraging the Adam algorithm to address this problem. We formulate a sophisticated multi-component loss function to simultaneously synthesize a flat-top main beam, deep multi-nulls, and stringent side-lobe level (SLL) control. Simulation results confirm that the Adam optimizer achieves superior convergence and stability compared with conventional gradient descent. Crucially, the solution preserves radiation pattern integrity even under practical discrete-phase quantization, demonstrating its viability for finite-resolution RIS hardware.**

Keywords: **Reconfigurable intelligent surface (RIS), beam pattern synthesis, Adam optimizer, phase quantization.**

I. Introduction

The evolution of sixth-generation (6G) wireless networks demands smart radio environments capable of real-time signal propagation reconfiguration. Reconfigurable Intelligent Surfaces (RIS) have emerged as a low-cost, passive solution to manipulate electromagnetic waves [1]. By adjusting element phase shifts, RIS enables complex beamforming such as multi-beam broadcasting and high-precision null-steering, essential for expanding coverage and mitigating co-channel interference in dense multi-user scenarios [2]. Early RIS research primarily optimized path loss and signal-to-noise ratio (SNR) for single-user setups [3], [4], [5], [6], [7]. However, modern interference-limited environments require simultaneous multi-beam synthesis and null-steering. Recent works have applied RIS to physical layer security by directing deep nulls toward eavesdroppers [8], [9],and to non-line-of-sight (NLOS) radar systems to enhance target detection and resolution [10], [11]. Despite these advancements, optimizing radiation patterns remains challenging due to the non-convex nature of beamforming under multiple simultaneous constraints. Conventional discrete phase shift designs and pattern synthesis algorithms [12] suffer from high computational overhead as the number of RIS elements scales up. While advanced beam synthesis algorithms mitigate this [13], the Adam optimizer offers remarkable efficiency due to its robust handling of sparse gradients and non-stationary objectives [14]. Furthermore, practical RIS deployments are constrained by low-resolution discrete phase shifters (e.g., 1-bit to 4-bit) to reduce hardware costs [15], which introduces severe distortions like increased sidelobe levels (SLL) and degraded null depths compared to traditional relays **direnzo2020reconfigurable**.

To address these challenges, this paper proposes a robust Adam-based beam- and null-steering optimization framework for RIS-aided communications. The main contributions are threefold: First, the proposed framework introduces an advanced adaptive learning mechanism that guarantees superior convergence stability for synthesizing complex flat-top and multi-narrow-beam configurations. Second, it quantifies the effects of practical 1-to-4-bit phase quantization, providing a comprehensive analysis of the trade-offs between hardware limitations, null depth, and beam precision. Third, extensive simulations demonstrate that our approach achieves deeper interference cancellation and more precise beam control than conventional methods while maintaining low computational complexity.

II. System Model

We consider an RIS-aided wireless communication system (Fig. 1) where an RIS reflects electromagnetic (EM) waves from a transmitter (Tx) toward desired users while mitigating interference to undesired users. The RIS is a uniform planar array (UPA) in the XOY plane with $N_{\text{RIS}} = M \times N$ elements, where M and N denote the

unit cell counts along the x- and y-axes, respectively, with spacing $d_x = d_y = d$. Each unit cell $n \in \{1, \ldots, N_{\text{RIS}}\}$

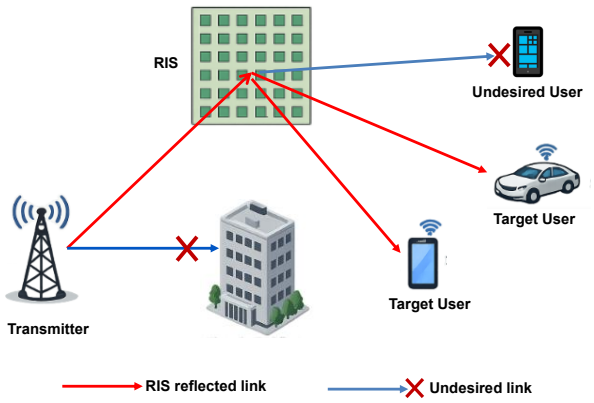

Fig. 1: RIS-aided wireless networks .

independently shifts the incident signal phase to steer the reflected beam. The spatial coordinates of the n-th element are defined by the vector $\mathbf{r}_n = [x_n, y_n, 0]^T$. The incident EM wave at the n-th RIS element is denoted as E_n^{inc}. Following phase modulation at each unit cell, the total reflected E-field at an observation angle (θ, ϕ) is expressed as:

$$\mathrm{E}^{re}(\theta, \phi; \mathbf{\Gamma}) = \sum_{n=1}^{N_{RIS}} g_n \, \Omega_0 e^{j\kappa \mathbf{r}_n^T \mathbf{u}(\theta,\phi)} E_n^{\text{inc}} = \mathbf{a}(\theta, \phi)^T \mathbf{\Gamma}, \tag{1}$$

where g_n is the reflection coefficient of the n-th unit cell, $\kappa = 2\pi/\lambda$ is the wavenumber, λ is the wavelength, $\mathbf{u}(\theta, \phi) = (\sin\theta\cos\phi, \sin\theta\sin\phi, \cos\theta)^T$ is the spherical unit directional vector, Ω_0 is the radiated E-field intensity of a single unit cell at a point of interest, $\mathbf{\Gamma}$ is the reflection coefficient vector of the RIS which is defined as

$$\mathbf{\Gamma} = [g_1, g_2, \ldots, g_{N_{\text{RIS}}}]^T, \tag{2}$$

and $\mathbf{a}(\theta, \phi)$ is array response vector that is

$$\mathbf{a}(\theta, \phi) = [a_1(\theta, \phi), a_2(\theta, \phi), \ldots, a_{N_{RIS}}(\theta, \phi)]^T, \tag{3}$$

and

$$a_n(\theta, \phi) = \Omega_0 \, e^{j\mathbf{k}\mathbf{r}_n^T \mathbf{u}(\theta,\phi)} \, E_n^{\text{inc}}. \tag{4}$$

The directivity of the reflected beam pattern from the RIS can be defined as one for an antenna array. The directivity toward the direction of (θ, ϕ) in the far-field zone can be defined as

$$D(\theta, \phi; \mathbf{\Gamma}) = \frac{4\pi \, |\mathrm{E}^{\text{re}}(\theta, \phi; \mathbf{\Gamma})|^2}{\displaystyle\int_{(\theta,\phi)\in\mathcal{M}} |\mathrm{E}^{\text{re}}(\theta, \phi; \mathbf{\Gamma})|^2 \sin\theta \, d\theta \, d\phi}. \tag{5}$$

We can rewrite (5) in Rayleigh Quotient form as

$$D(\theta, \phi; \mathbf{\Gamma}) = \frac{\mathbf{\Gamma}^H \mathbf{A}(\theta, \phi) \mathbf{\Gamma}}{\mathbf{\Gamma}^H \mathbf{Q} \mathbf{\Gamma}}, \tag{6}$$

where

$$\mathbf{A}(\theta, \phi) = \mathbf{a}(\theta, \phi) \, \mathbf{a}(\theta, \phi)^H, \tag{7}$$

and

$$\mathbf{Q} = \frac{1}{4\pi} \int_{\theta,\phi\in\mathcal{M}} \mathbf{a}(\theta, \phi)\mathbf{a}(\theta, \phi)^H \sin\theta \, d\theta \, d\phi. \tag{8}$$

In (8), $\mathcal{M} = \{(\theta, \phi) \mid 0 \le \theta \le \pi/2, \ -\pi \le \phi \le \pi\}$ is the upper hemisphere radiation region of the RIS.

From (6), the RIS directivity depends primarily on the array configuration $\mathbf{a}(\theta, \phi)$ and the reflection coefficient vector $\mathbf{\Gamma}$. Under the unit-modulus constraint $|g_n| = 1$, each coefficient is parameterized by a real phase variable φ_n as $g_n = e^{j\varphi_n}$. Consequently, we focus on optimizing the phase vector $\boldsymbol{\varphi} = [\varphi_n, \ldots, \varphi_{N_{\text{RIS}}}]^T$ to achieve the target radiation patterns.

III. Adam Based RIS Reflection Pattern Synthesis

A. Objective Function

To synthesize the desired patterns under the unit-modulus constraint $g_k = e^{j\varphi_k}$, we optimize the phase vector $\boldsymbol{\varphi}$ directly. The composite objective function to be minimized is given by:

$$L_{total}(\boldsymbol{\varphi}) = L_{beam}(\boldsymbol{\varphi}) + \lambda_{null} \, L_{null}(\boldsymbol{\varphi}) + \lambda_{sll} \, L_{sll}(\boldsymbol{\varphi}), \tag{9}$$

where $\boldsymbol{\varphi}$ is the reflection phase vector of RIS, λ_{null} and λ_{sll} are positive weighting coefficients that balance the trade-off between main beam formation, null steering, and sidelobe level control, and $L_{beam}, L_{null}, L_{sll}$ are the per-region sub-losses defined as

$$L_{beam}(\boldsymbol{\varphi}) = \frac{1}{M_b} \sum_{(\theta,\phi)\in\Omega_{flat}} \left(D(\theta, \phi; \mathbf{\Gamma}(\boldsymbol{\varphi})) - \alpha\right)^2, \tag{10}$$

$$L_{null}(\boldsymbol{\varphi}) = \frac{1}{M_n} \sum_{(\theta,\phi)\in\Omega_{null}} D(\theta, \phi; \mathbf{\Gamma}(\boldsymbol{\varphi})), \tag{11}$$

$$L_{sll}(\boldsymbol{\varphi}) = \frac{1}{M_s} \sum_{(\theta,\phi)\in\Omega_{sll}} \max(0, \, D(\theta, \phi; \mathbf{\Gamma}(\boldsymbol{\varphi})) - \tau)^2. \tag{12}$$

Here, M_b, M_n, and M_s denote the number of sampling points within the flat-top (Ω_{flat}), null (Ω_{null}), and SLL (Ω_{sll}) regions, respectively. The vector $\mathbf{\Gamma}(\boldsymbol{\phi})$ represents the phase-dependent reflection coefficients. The parameter α is the target directivity in the flat-top region, while τ is the predefined threshold penalizing only the sidelobes

that exceed the permitted level. Because each sub-loss $L_x(\boldsymbol{\phi})$ is fully differentiable, the gradient of L_{total} can be efficiently computed.

B. Adaptive Moment Estimation Algorithm

To solve the non-convex problem of minimizing $L_{total}(\boldsymbol{\varphi})$ under the unit-modulus constraint, we adopt an Adam-based optimization scheme. The key idea is to perform updates directly on the real-valued phase vector $\boldsymbol{\varphi} \in R^{N_{RIS}}$ and recover the unit-modulus reflection coefficients via $g_k = e^{j\varphi_k}$, so that the constraint $|g_k| = 1$ is automatically satisfied. The derivative of the real-valued loss L_{total} with respect to the real variable φ_k is obtained from the derivative with respect to the complex variable g_k as

$$\frac{\partial L_{total}}{\partial \varphi_k} = \frac{\partial L_{total}}{\partial g_k}\frac{dg_k}{d\varphi_k} + \frac{\partial L_{total}}{\partial g_k^*}\frac{dg_k^*}{d\varphi_k}. \tag{13}$$

Given that $\dfrac{dg_k}{d\varphi_k} = jg_k$, after transformation, we obtain

$$\frac{\partial L_{total}}{\partial \varphi_k} = 2\,\mathrm{Im}\left(g_k \cdot \frac{\partial L_{total}}{\partial g_k}\right), \tag{14}$$

where $\dfrac{\partial L_{total}}{\partial g_k}$ is the complex-valued gradient obtained by summing the corresponding gradient of L_{beam}, $\lambda_{null}L_{null}$, and $\lambda_{sll}L_{sll}$ with respect to g_k.

The reflection phase vector at $\boldsymbol{\varphi}$ is then updated using the Adam optimizer. Denoting the gradient at iteration t by $\mathbf{g}^{(t)} = \nabla_{\boldsymbol{\varphi}} L_{total}|_{\boldsymbol{\varphi}=\boldsymbol{\varphi}^{(t-1)}}$, the first moment vector $\mathbf{m}^{(t)}$ and second moment vector $\mathbf{s}^{(t)}$ are recursively updated as

$$\mathbf{m}^{(t)} = \beta_1 \mathbf{m}^{(t-1)} + (1-\beta_1)\,\mathbf{g}^{(t)}, \tag{15}$$

$$\mathbf{s}^{(t)} = \beta_2 \mathbf{s}^{(t-1)} + (1-\beta_2)\,(\mathbf{g}^{(t)})^2, \tag{16}$$

where β_1 and β_2 denote the exponential decay rates for the first- and second-order moment estimates, respectively. To counteract the initialization bias towards zero, the bias-corrected moment estimates are computed as

$$\hat{\mathbf{m}}^{(t)} = \frac{\mathbf{m}^{(t)}}{1-\beta_1^t}, \tag{17}$$

$$\hat{\mathbf{s}}^{(t)} = \frac{\mathbf{s}^{(t)}}{1-\beta_2^t}. \tag{18}$$

Finally, the phase vector is updated as

$$\boldsymbol{\varphi}^{(t)} = \boldsymbol{\varphi}^{(t-1)} - \eta_t \frac{\hat{\mathbf{m}}^{(t)}}{\sqrt{\hat{\mathbf{s}}^{(t)}} + \epsilon}, \tag{19}$$

where ϵ is a small positive constant introduced to avoid division by zero and improve arithmetic stability, and η_t is the time-varying learning rate following a cosine annealing schedule:

$$\eta_t = \frac{\eta_0}{2}\left[1 + \cos\left(\frac{\pi t}{T_{max}}\right)\right], \tag{20}$$

with η_0 being the initial learning rate and T_{max} the maximum number of iterations. The cosine schedule is adopted because it uses a relatively large step in the early iterations to facilitate exploration of the highly non-convex phase landscape, and then gradually shrinks the step toward the end of training to enable fine-grained refinement around the optimum, thereby improving final accuracy and avoiding oscillations near convergence.

To accelerate convergence, the initial phase $\varphi_k^{(0)}$ is set based on the centroid $(\bar{\theta}, \bar{\phi})$ of the target beam region Ω^b in the angular domain, augmented with a quadratic spatial taper:

$$\begin{aligned}\varphi_k^{(0)} = {} & k\left(x_k \sin\bar{\theta}\cos\bar{\phi} + y_k \sin\bar{\theta}\sin\bar{\phi}\right) \\ & + \gamma\left[(x_k-\bar{x})^2 + (y_k-\bar{y})^2\right],\end{aligned} \tag{21}$$

where $\kappa = 2\pi/\lambda$ is the wavenumber providing the linear progressive phase that steers the main beam toward $(\bar{\theta}, \bar{\phi})$, $(\bar{x}, \bar{y})$ is the array's geometric center, and γ is the second-order attenuation coefficient acting as a beam-broadening factor.

Following the continuous optimization, the optimized phase $\varphi_k^{(*)}\varphi_k^{(T_{max})}$ must be mapped to a B-bit discrete set $\mathcal{P}_B = \left\{\frac{2\pi n}{2^B}\right\}_{n=0}^{2^B-1}$ due to hardware constraints. The final quantized phase $\varphi_k^{(q)}$ is obtained by

$$\varphi_k^{(q)} = \arg\min_{p\in\mathcal{P}_B}\left|\varphi_k^{(*)} \bmod 2\pi - p\right|, \tag{22}$$

and the corresponding hardware-realizable reflection coefficient is reconstructed as $g_k^{(q)} = e^{j\varphi_k^{(q)}}$. The full procedure is detailed in Algorithm 1.

IV. Simulation Results and Validation

This section evaluates the proposed Adam-based optimization method regarding convergence, beamforming accuracy, and null-steering capability against the conventional gradient descent (GD) method. We also analyze learning rate sensitivity, phase quantization effects, and multi-beam/multi-null synthesis. We consider a 20×20 planar RIS with element spacing $d = \lambda/2$. The incident wave direction is $(\theta_i, \phi_i) = (25^\circ, -40^\circ)$, and the maximum iterations are $T_{\max} = 1000$. Adam parameters are configured as $\beta_1 = 0.9$, $\beta_2 = 0.999$, and $\epsilon = 10^{-8}$ [12]. Based on the sensitivity analysis in Section IV-A, the initial learning rate is $\eta_0 = 0.3$. The beam-broadening factor and SLL threshold are $\gamma = 0.3$ and $\tau = 0.8$,

Algorithm 1 Adam-based RIS Beam Pattern Synthesis

Require:
System parameters: $M, N, (\theta_i, \phi_i), \Omega^b, \Omega^n, \Omega^{sll}, B$
Loss parameters: α, τ
Optimization weights: $\lambda_{null}, \lambda_{sll}$
Adam hyperparameters: $T_{max}, \eta_0, \beta_1, \beta_2, \epsilon$
Ensure: Quantized phase vector $\boldsymbol{\varphi}^{(q)}$ and reflection coefficients $\boldsymbol{\Gamma}^{(q)}$

Initialize $\boldsymbol{\varphi}^{(0)}$ via (21), $\mathbf{m}^{(0)} \leftarrow \mathbf{0}, \mathbf{s}^{(0)} \leftarrow \mathbf{0}$
for $t = 1$ to T_{max} **do**
  Compute gradients $\nabla_{\boldsymbol{\varphi}} L_{beam}$, $\nabla_{\boldsymbol{\varphi}} L_{null}$, $\nabla_{\boldsymbol{\varphi}} L_{sll}$ at $\boldsymbol{\varphi}^{(t-1)}$ using (14)
  $\mathbf{g}^{(t)} \leftarrow \nabla_{\boldsymbol{\varphi}} L_{beam} + \lambda_{null} \nabla_{\boldsymbol{\varphi}} L_{null} + \lambda_{sll} \nabla_{\boldsymbol{\varphi}} L_{sll}$
  $\mathbf{m}^{(t)} \leftarrow \beta_1 \mathbf{m}^{(t-1)} + (1-\beta_1)\,\mathbf{g}^{(t)}$
  $\mathbf{s}^{(t)} \leftarrow \beta_2 \mathbf{s}^{(t-1)} + (1-\beta_2)\,(\mathbf{g}^{(t)} \odot \mathbf{g}^{(t)})$
  $\hat{\mathbf{m}}^{(t)} \leftarrow \mathbf{m}^{(t)}/(1-\beta_1^t), \quad \hat{\mathbf{s}}^{(t)} \leftarrow \mathbf{s}^{(t)}/(1-\beta_2^t)$
  Update η_t via (20)
  $\boldsymbol{\varphi}^{(t)} \leftarrow \boldsymbol{\varphi}^{(t-1)} - \eta_t\, \hat{\mathbf{m}}^{(t)}/(\sqrt{\hat{\mathbf{s}}^{(t)}} + \epsilon)$
end for
Quantize: $\varphi_k^{(q)} \leftarrow \arg\min_{p \in \mathcal{P}_B} |\varphi_k^{(T_{max})} \bmod 2\pi - p|$
Reconstruct: $g_k^{(q)} \leftarrow e^{j\varphi_k^{(q)}}$, $\boldsymbol{\Gamma}^{(q)} \leftarrow [g_1^{(q)}, \ldots, g_{N_{RIS}}^{(q)}]^T$
return $\boldsymbol{\varphi}^{(q)}, \boldsymbol{\Gamma}^{(q)}$

respectively, with weighting factors λ_{null} and λ_{sll} tuned to balance sub-loss terms. These default settings apply throughout this section unless specified otherwise.

A. Convergence Behavior Analysis

We evaluate the proposed Adam algorithm against the traditional GD method for simultaneous main lobe synthesis and null generation, including an investigation into the initial learning rate (η_0) sensitivity. As shown in Fig. 2(a) with $\eta_0 = 0.3$, Adam exhibits superior convergence speed and accuracy over GD. While both algorithms initialize at a loss of ∼38 dB, Adam drops below 30 dB within 140 iterations, whereas GD requires nearly 500 iterations. By the 1000th iteration, Adam achieves a stable state at ∼24.2 dB, outperforming GD's 28.3 dB. This demonstrates Adam's capacity to both accelerate convergence and escape poor local optima.

Fig. 2(b) illustrates the impact of η_0 on Adam's convergence rate and optimization stability. Setting $\eta_0 \in [0.2, 0.4]$ yields the best performance, striking an optimal balance between fast objective reduction and low steady-state error. Because $\eta_0 = 0.3$ offers the most stable and efficient optimization trajectory, it is selected as the default baseline for all subsequent simulation scenarios.

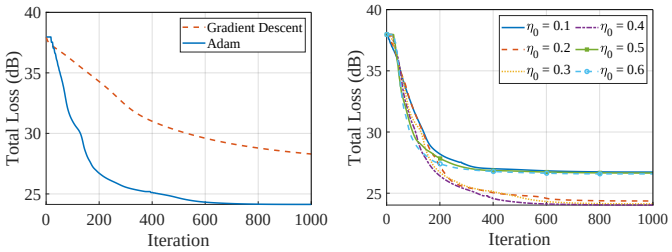

(a) (b)

Fig. 2: Convergence comparison between: (a) GD and Adam; (b) Impact of Adam's learning rate (η_0).

B. Beam and Null Formation

To evaluate beam and null formation, we set the target beam region to $\Omega^b = \{(\theta, \phi) \mid 40° \le \theta \le 60°, 50° \le \phi \le 80°\}$ and the null region to $\Omega^n = \{(\theta, \phi) \mid 65° \le \theta \le 80°, 100° \le \phi \le 120°\}$ using a 4-bit RIS (16 phase levels). The normalized directivity in the (θ, ϕ) plane (Fig. 3) confirms that the proposed algorithm effectively synthesizes the desired pattern. A ∼40 dB isolation between the main beam and the null point ensures reliable data transmission for legitimate users while thoroughly suppressing interference at the null region.

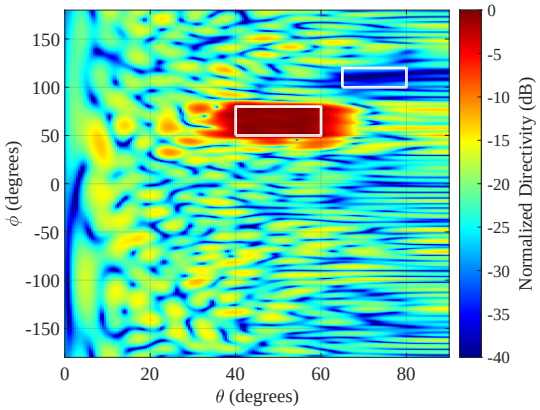

Fig. 3: Normalized directivity on the (θ, ϕ) plane.

Fig. 4 details the pattern cuts sampled at the midpoints of the predefined angular regions to assess flatness and suppression depth. Fig. 4(a) shows a stable main beam across $40° \le \theta \le 60°$ (at $\phi = 65°$) alongside a deep null below -40 dB at the specified interference direction ($65° \le \theta \le 80°$ at $\phi = 110°$). Fig. 4(b) illustrates precise radiation focusing within $50° \le \phi \le 80°$, with sidelobes suppressed below -15 dB, thereby maximizing signal strength and minimizing leakage.

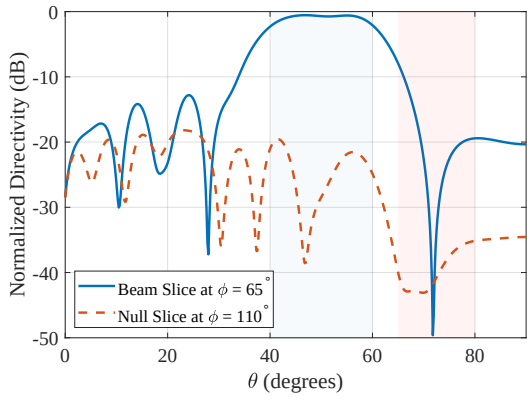

(a)

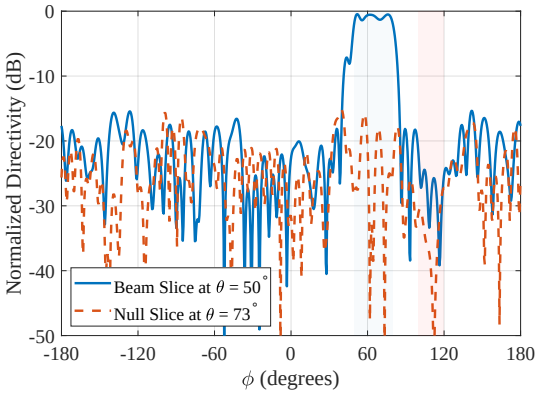

(b)

Fig. 4: Normalized directivity distribution of RIS with beam and null pattern: (a) Cross-section along the elevation angle θ at fixed ϕ; (b) Cross-section along the azimuth angle ϕ at fixed θ.

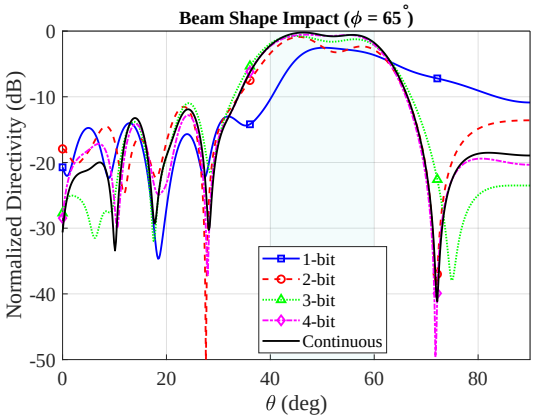

(a)

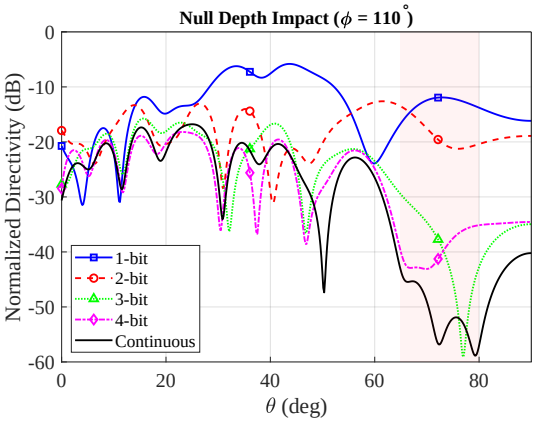

(b)

Fig. 5: Fig. 5: Phase quantization effects on RIS radiation performance: (a) beam shape distortion at $\phi = 65°$, and (b) null depth attenuation at $\phi = 110°$.

To analyze phase quantization impacts, we evaluated 1- to 4-bit resolutions (2, 4, 8, and 16 levels) against the ideal continuous-phase baseline. As shown in Fig. 5(a), 1-bit quantization significantly degrades directivity and distorts the main beam, whereas the 4-bit curve closely converges to the continuous-phase ideal. Similarly, Fig. 5(b) highlights the impact on null-steering accuracy: 1-bit and 2-bit cases fail to suppress interference, exhibiting directivity above 0 dB. In contrast, the 4-bit configuration achieves a suppression depth near -40 dB, matching the continuous-phase performance.

C. Multiple Beam-Null

Finally, the capability to generate multiple concurrent beams and cancellation points using a 4-bit RIS (16 levels) is verified. Specifically, we target two distinct beam regions: $\Omega_{b1} = \{(\theta, \phi) \mid 10° \leq \theta \leq 20°, 50° \leq \phi \leq 70°\}$ and $\Omega_{b2} = \{(\theta, \phi) \mid 50° \leq \theta \leq 60°, 50° \leq \phi \leq 70°\}$, alongside two null regions: $\Omega_{n1} = \{(\theta, \phi) \mid 20° \leq \theta \leq 30°, -50° \leq \phi \leq -30°\}$ and $\Omega_{n2} = \{(\theta, \phi) \mid 40° \leq \theta \leq 50°, -50° \leq \phi \leq -30°\}$. As demonstrated in Fig. 6, the proposed framework successfully synthesizes both beams and nulls with high precision, perfectly matching all predefined angular constraints.

V. Conclusion

This paper successfully synthesizes RIS radiation patterns using the Adam optimization algorithm. By employing a multi-component objective function, the proposed framework effectively balances flat-top main beam formation, multi-null interference cancellation, and sidelobe level (SLL) control. Furthermore, Adam's adaptive learning rate mechanism ensures stable, high-accuracy convergence under practical discrete phase quantization constraints. These findings confirm the feasibility and robustness of the proposed optimization framework for finite-

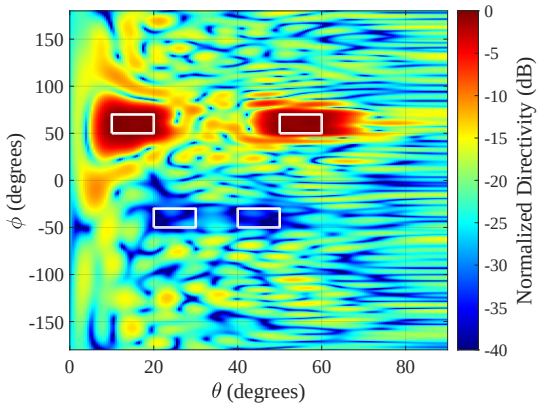

Fig. 6: Normalized directivity of the RIS-assisted pattern with multiple beams and multiple nulls.

resolution RIS deployments in next-generation wireless networks.

ACKNOWLEDGMENT

Nguyen Minh Tran was funded by the Post-Doctoral Scholarship Programme of Vingroup Innovation Foundation (VINIF), code [VINIF.2025.STS.01].

REFERENCES

[1] ElMossallamy et al., "Reconfigurable intelligent surfaces for wireless communications: Principles, challenges, and opportunities," *IEEE Trans. Cogn. Commun. Netw.*, vol. 6, no. 3, pp. 990–1002, 2020.

[2] Q. Wu and R. Zhang, "Towards smart and reconfigurable environment: Intelligent reflecting surface aided wireless network," *IEEE Commun. Mag.*, vol. 58, no. 1, pp. 106–112, 2020.

[3] W. Tang et al., "Wireless communications with reconfigurable intelligent surface: Path loss modeling and experimental measurement," *IEEE Trans. Wirel. Commun.*, vol. 20, no. 1, pp. 421–439, 2021.

[4] C. Huang, R. Mo, and C. Yuen, "Reconfigurable intelligent surface assisted multiuser MISO systems exploiting deep reinforcement learning," *IEEE J. Sel. Areas Commun.*, vol. 38, no. 8, pp. 1839–1850, 2020.

[5] Q. Wu and R. Zhang, "Intelligent reflecting surface enhanced wireless network via joint active and passive beamforming," *IEEE Trans. Wirel. Commun.*, vol. 18, no. 11, pp. 5394–5409, 2019.

[6] S. Hu et al., "Beyond massive MIMO: The potential of data transmission with large intelligent surfaces," *IEEE Trans. Signal Process.*, vol. 66, no. 10, pp. 2746–2758, 2018.

[7] I. Singh, P. J. Smith, and P. A. Dmochowski, "Optimal SNR analysis for single-user RIS systems," *arXiv preprint arXiv:2008.09376*, 2021.

[8] M. Cui, G. Zhang, and R. Zhang, "Secure wireless communication via intelligent reflecting surface," *IEEE Wirel. Commun. Lett.*, vol. 8, no. 5, pp. 1410–1414, 2019.

[9] R. Kaur and B. Bansal, "Secure beamforming for intelligent reflecting surface assisted MISO wireless communications," in *Proc. 3rd Int. Conf. Intell. Commun. Comput. Tech. (ICCT)*, 2023, pp. 1–5.

[10] J. Ye, Y. Peng, et al., "RIS-assisted radar NLOS target detection," in *2022 5th International Conference on Information Communication and Signal Processing (ICICSP)*, 2022, pp. 630–635.

[11] M. V. Vejling et al., "RIS-assisted high resolution radar sensing," *IEEE Trans. Signal Process.*, vol. 73, pp. 2940–2955, 2025.

[12] W. Wang and other, "Integer-based pattern synthesis for asymmetric multi-reflection RIS," in *2024 IEEE Wireless Communications and Networking Conference (WCNC)*, 2024, pp. 1–6.

[13] N. T. Toan, T. V. B. Giang, and N. M. Tran, "A versatile beam synthesis algorithm for reflection beam formation of RIS-aided wireless networks," *VNU Journal of Science: Computer Science and Communication Engineering*, vol. 41, no. 1, pp. 84–96, 2025.

[14] D. P. Kingma and J. Ba, "Adam: A method for stochastic optimization," *arXiv preprint arXiv:1412.6980*, 2014.

[15] P. Xu, G. Chen, Z. Yang, and M. Di Renzo, "Reconfigurable intelligent surfaces-assisted communications with discrete phase shifts: How many quantization levels are required to achieve full diversity?" *IEEE Wirel. Commun. Lett.*, vol. 10, no. 2, pp. 358–362, 2021.